Shortened Current Injection for Sensorless Switched Reluctance Motor Drives Based on High-Sensitivity-Region-Optimized Position Observer

Zifeng Chen, *Graduate Student Member, IEEE*, Xijian Lin, Dehui Luo, *Graduate Student Member, IEEE*, Molong Duan, *Member, IEEE*, Shun Cai, *Member, IEEE*, and Dianxun Xiao, *Senior Member, IEEE*

***Abstract*—Conventional pulse injection-based phase-locked loop (PLL) enables full-cycle position estimation for low-speed sensorless switched reluctance motor (SRM) control without magnetic data but faces high injection current and low accuracy with its performance limitations related to inductance sensitivity characteristics. In particular, in the high-sensitivity region (HSR), where the rate of change of inductance with position is high, even a slight inductance disturbance can lead to an unexpected position estimation error. To address these challenges, this article proposes an improved position observer considering the high sensitivity region of phase inductance. By introducing the optimized heterodyne method, the use of high-sensitivity low-inductance regions for position estimation is avoided, thereby enhancing position estimation accuracy. Furthermore, the proposed method can estimate the full-cycle position with a shorter injection interval, reducing the injection current amplitude. Finally, experiments conducted on a three-phase 750 W SRM setup validate the feasibility and effectiveness of the proposed scheme. Compared with the conventional scheme, this scheme reduces the peak value of the injected current by up to 63% and improves the estimation accuracy by 50%, thereby demonstrating desirable estimation performance while reducing power losses.**

***Index Terms*—Low-speed operation, machine inductance, pulse injection, sensorless control, switched reluctance motor (SRM).**

Received 8 August 2025; revised 6 December 2025 and 2 February 2026; accepted 12 March 2026. Date of publication 23 March 2026; date of current version 22 July 2026. This work was supported in part by the National Natural Science Foundation of China under Grant 52307069, in part by Guangdong Science and Technology Program under Grant 2025A0505020029, in part by the Youth S&T Talent Support Programme of Guangdong Provincial Association for Science and Technology (GDSTA) under Grant SKXRC2025465, and in part by the Project of Hetao Shenzhen-Hong Kong Science and Technology Innovation Cooperation Zone under Grant HZQB-KCZYB-2020083. *(Corresponding author: Dianxun Xiao.)*

Zifeng Chen, Xijian Lin, and Dehui Luo are with the Sustainable Energy and Environment Thrust, The Hong Kong University of Science and Technology (Guangzhou), Guangzhou 511453, China.

Molong Duan is with the Department of Mechanical and Aerospace Engineering, The Hong Kong University of Science and Technology, Hong Kong, SAR, China.

Shun Cai is with the College of Electrical Engineering, Zhejiang University, Hangzhou 310027, China.

Dianxun Xiao is with the Sustainable Energy and Environment Thrust, The Hong Kong University of Science and Technology (Guangzhou), Guangzhou 511453, China, also with The Hong Kong University of Science and Technology, Hong Kong, SAR, China, and also with HKUST Shenzhen–Hong Kong Collaborative Innovation Research Institute, Shenzhen 518048, China (e-mail: dianxunxiao@hkust-gz.edu.cn).

Digital Object Identifier 10.1109/TTE.2026.3676844

I. INTRODUCTION

AMID the global transition toward zero-emission transportation, switched reluctance motors (SRMs) are gaining increasing attention for their applications in electric vehicles, electric aircraft, and electric ships [1]. With inherent advantages such as high reliability, durability, low cost, and independence from rare earth materials, SRMs are particularly well suited for transportation electrification scenarios that demand supply chain resilience and reliable performance under harsh operating conditions [2], [3]. To achieve high-performance control of SRMs, accurate rotor position information is essential, which typically requires the installation of position sensors. Position sensors are generally classified into incremental encoders, absolute encoders, and resolvers [4], [5], [6]. The incorporation of position sensors in motors results in increased volume and higher costs [7], [8]. Therefore, the development of sensorless control techniques for SRMs has become a crucial area of research.

Currently, sensorless control research primarily focuses on high-speed operating conditions. Common control schemes include flux linkage characteristic methods [9], [10], observer-based control methods [11], [12], [13], [14], [15], [16], and intelligent algorithms [17], [18], [19]. However, for low-speed operation, where these approaches may not be as effective due to the low signal-to-noise ratio, the pulse injection method is widely recognized as an effective sensorless control scheme [20], [21], [22], [23], [24], [25], [26], [27], [28], [29], [30], [31], [32], [33], [34].

In injection methods, the lookup table-based method provides a simple way to obtain the rotor position [20], [21]. By comparing the flux linkage generated by the injection method with a preset special flux linkage, the rotor's position region and phase conduction state can be further determined [22]. To eliminate the need for pre-measuring unsaturated inductance characteristics at low speeds, a dual-phase current chopping combined with a characteristic-position interpolation-based online self-tuning scheme is proposed. However, this method still suffers from deviations in inductance modeling near the aligned and unaligned positions [23]. Additionally, the single-current threshold method [24] estimates the position based on the current threshold and improves the estimation accuracy by combining the current gradient change. An online least squares method is proposed to fit current samples and dynamically adjust the injected current, preventing the current from exceeding the threshold during the injection process [25]. The linear interval method is introduced to estimate the position, addressing the issue of inductance imbalance; however, this method performs poorly under load conditions [26]. To further reduce implementation cost, a low-cost triple current slope difference threshold method [27] has been proposed. However, this approach relies on zero-current prediction, which requires intensive computation and yields higher estimation error under heavy-load conditions.

To improve load adaptability at low speeds, the robustness of the control method is enhanced by calculating the self-inductance value based on the saturated inductance characteristics of the SRM [28]. In [29], the rotor position is estimated by detecting the inflection points of the inductance curve. However, this approach necessitates precise modeling and measurement of the magnetic characteristics, which is a common limitation of the pulse injection method due to its dependence on prior parameter measurements. Several studies have proposed sensorless control methods that do not rely on such parameters [30], [31], [32], [33], [34]. For instance, the full-cycle inductance method in [30] determines position and commutation moments based on inductance crossover points, but it is ineffective when the SRM operates in the saturation region. A position estimation method using inductance crossover points combined with a phase-locked loop (PLL) for filtering is proposed. However, this method is limited by the PLL bandwidth and is unsuitable during saturation or start-up phases [31]. The region-based PLL (RPLL)-based pulse injection scheme is proposed, offering strong robustness, but it has a complex structure, and its control accuracy remains average [32]. Further research proposed by Xiao et al. [33] and Lv et al. [34] offers revised versions of the RPLL, optimizing injected current amplitude and audible noise, respectively. Unfortunately, these improvements do not enhance estimation accuracy.

Therefore, this article proposes an enhanced sensorless control scheme based on high-sensitivity-region-optimized (HSRO) heterodyne processing. Conventional high-frequency pulse injection (HFPI) methods [32], [34], when applied without considering magnetic characteristics, are limited by two main factors: low estimation accuracy, where the position error becomes unacceptably large due to the sensitivity of inductance to small disturbances, and excessive power losses, where the injection current amplitude is large enough to cause power dissipation, leading to inefficiency and potential thermal issues in the system. In comparison, the proposed method has the following advantages.

1) Address accuracy degradation caused by excessive parameter sensitivity, thereby improving position estimation accuracy, which is a limitation of several existing sensorless schemes [30], [31], [32].
2) Reduce the injection interval to avoid unnecessary injections, reduce the injection current peak value, extend motor lifespan, and make the motor operation more stable and reliable.

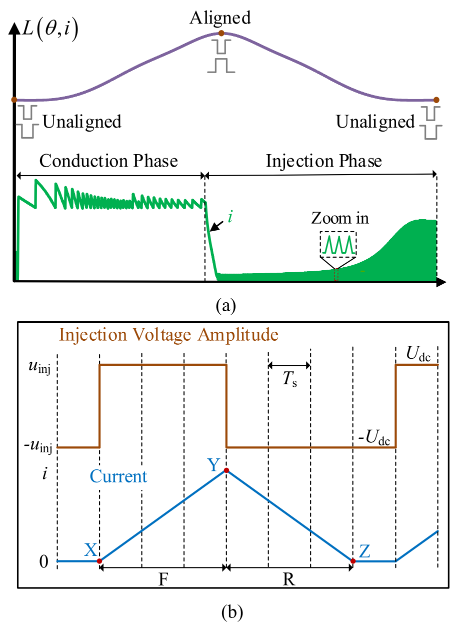

Fig. 1. Conventional pulse-injection-based sensorless control scheme. (a) Phase current and phase inductance. (b) Injection voltage and induced pulse current.

Finally, extensive experiments conducted on a 750 W three-phase SRM test setup verify the effectiveness and reliability of the proposed sensorless control algorithm.

II. Conventional Pulse Injection-Based RPLL Sensorless Control Method

A. Basic Principle of the RPLL Sensorless Control Scheme

Low-speed sensorless control of the SRM is usually achieved by HFPI. During this process shown in Fig. 1, hysteresis control in the soft chopping mode is adopted to regulate the current when the phase is conducting. In the idle stage, high-frequency injections containing a pair of forward (F) and reverse (R) voltage pulses are enabled. The injection amplitude is set as the DC link voltage U_{DC}, and the current sampling period is defined as T_s. To ensure that the induced current i decays to zero before the start of the next positive voltage pulse, an additional negative voltage pulse is added.

With a short injection time, the low-induced current allows magnetic saturation to be ignored. The phase inductance within a pair of forward and reverse voltage pulses is unchanged. Hence, the SRM model can be expressed as [32]

$$U_{\mathrm{DC}} = Ri + L(\theta)\left.\frac{di}{dt}\right|_{\mathrm{F}} + i\omega\frac{dL(\theta)}{d\theta} \tag{1}$$

$$-U_{\mathrm{DC}} = Ri + L(\theta)\left.\frac{di}{dt}\right|_{\mathrm{R}} + i\omega\frac{dL(\theta)}{d\theta} \tag{2}$$

where R stands for stator resistance, $L(\theta)$ is a function of the position angle θ, representing the inductance of the SRM, and its value varies with the rotor position θ, di/dt indicates the derivative of the current i for time t, that is, the rate of change of current. ω represents the mechanical rotor, and $dL(\theta)/d\theta$ is the derivative of the inductance $L(\theta)$ for the rotor position θ, indicating the rate of change of inductance with the rotor position. The inherent symmetry of positive and negative voltage pulse injection enables mutual cancellation of the average ohmic voltage drop and back electromotive force over a pulse period, thereby decoupling the position-dependent inductance term for precise rotor position estimation [33]. According to Fig. 1(b), the inductance of the idle phase can be obtained through (1) and (2)

$$L(\theta)|_{\text{idle}} = \frac{2U_{\text{DC}}}{\frac{di}{dt}\big|_{\text{F}} - \frac{di}{dt}\big|_{\text{R}}} = \frac{2U_{\text{DC}} \cdot 3T_{\text{s}}}{2i_{\text{Y}} - i_{\text{X}} - i_{\text{Z}}} \tag{3}$$

where i_{Y}, i_{X}, and i_{Z} represent the sampled currents at different moments.

Subsequent position-sensorless control can be achieved by estimating rotor position from inductance through the RPLL pulse injection scheme [32], [33]. To accurately utilize this principle for position-sensorless control, it is crucial to understand the nonsaturated inductance characteristics. The nonsaturated inductance characteristics calculated using the HFPI method can be characterized by constructing an equivalent model consisting of DC component L_0, fundamental component L_1, and second harmonic component L_2 with its mathematical expression presented as follows:

$$\begin{cases} L_A = L_0 - L_1\cos(N_r\theta) - \hat{L}_2\cos\left(2N_r\hat{\theta}\right) \\ L_B = L_0 - L_1\cos\left(N_r\theta - \dfrac{2\pi}{3}\right) \\ \qquad - \hat{L}_2\cos\left(2\left(N_r\hat{\theta} - \dfrac{2\pi}{3}\right)\right) \\ L_C = L_0 - L_1\cos\left(N_r\theta + \dfrac{2\pi}{3}\right) \\ \qquad - \hat{L}_2\cos\left(2\left(N_r\hat{\theta} + \dfrac{2\pi}{3}\right)\right) \end{cases} \tag{4}$$

where N_r denotes rotor pole count. The estimated values of L_0 and L_1 can be obtained through the look-up table method or using the self-tuning scheme of inductance [32], denoted as $\hat{L}_0$, $\hat{L}_1$, and $\hat{L}_2$.

By using the parameters obtained from the self-tuning method or the look-up table method, the uncertain parameters in the derived idle-phase inductance can be eliminated, which gives

$$\begin{cases} L_{AN} = \dfrac{L_A - \hat{L}_0 - \hat{L}_2\cos\left(2N_r\hat{\theta}\right)}{\hat{L}_1} = -\cos(N_r\theta) \\ L_{BN} = \dfrac{L_B - \hat{L}_0 - \hat{L}_2\cos\left(2\left(N_r\hat{\theta} - \frac{2\pi}{3}\right)\right)}{\hat{L}_1} \\ \qquad = -\cos\left(N_r\theta - \dfrac{2\pi}{3}\right) \\ L_{CN} = \dfrac{L_C - \hat{L}_0 - \hat{L}_2\cos\left(2\left(N_r\hat{\theta} + \frac{2\pi}{3}\right)\right)}{\hat{L}_1} \\ \qquad = -\cos\left(N_r\theta + \dfrac{2\pi}{3}\right) \end{cases} \tag{5}$$

where L_{AN}, L_{BN}, and L_{CN} denote the three-phase normalized idle inductance. The idle phase inductance characteristics of a three-phase 12/8 SRM based on the RPLL sensorless control scheme are shown in Fig. 2. Here, θ_{on} and θ_{off} denote the turn-on angle and turn-off angle, respectively.

In the RPLL sensorless control scheme, the rotor position is reconstructed by converting the normalized idle inductance into heterodyne signals. To ensure continuous observability across a full electrical period, the SRM's operation is divided into two regions. According to [32], combining the idle inductances of two adjacent phases in region I, and those of a single phase in region II yields the heterodyne signal $e_{\_RPLL}$, with position estimation through PLL enabling sensorless control.

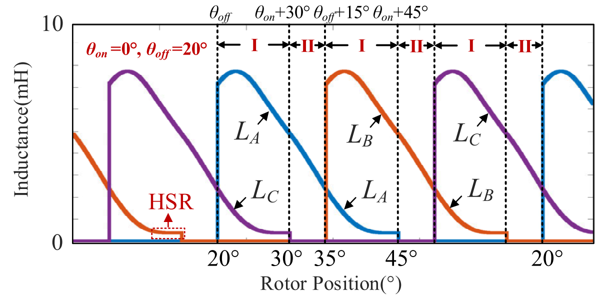

Fig. 2. Idle phase inductance characteristics of a three-phase 12/8 SRM based on the RPLL sensorless control scheme.

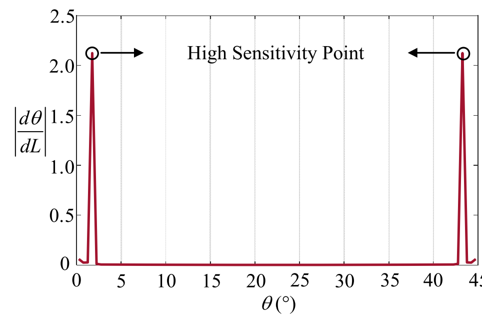

Fig. 3. Sensitivity curve of $|d\theta/dL|$ with respect to θ.

B. Limitations and Drawbacks of the RPLL Sensorless Scheme

Although the RPLL scheme enables sensorless control without relying on magnetic characteristics and offer qualified filtering performance, two critical limitations and drawbacks hinder its practical deployment in high-precision and low-loss applications.

The first limitation of the RPLL scheme is its poor estimation accuracy. This arises from the high sensitivity in regions with small inductance values, which lead to larger position estimation errors. Specifically, $|d\theta/dL|$ is highly responsive to changes in inductance L. A detailed sensitivity analysis of the parameter is as follows.

Mathematically, $|d\theta/dL|$ represents the rate at which the rotor position θ changes with respect to the inductance L. When $|d\theta/dL|$ is large, even a small change in inductance $\Delta L_{\text{sens.}}$, which arises from sampling noise or temperature drift, can cause a change in position $\Delta\theta_{\text{sens.}}$, which can be expressed as

$$\Delta\theta_{\text{sens.}} = \left|\frac{d\theta}{dL}\right| \cdot \Delta L_{\text{sens.}}. \tag{6}$$

To visualize this relationship, Fig. 3 is derived from the inductance-position characteristics shown in Fig. 1 by numerically calculating the sensitivity function $|d\theta/dL|$. This curve reflects how the inductance sensitivity varies with respect to rotor position. As illustrated in Fig. 3, the curve of $|d\theta/dL|$

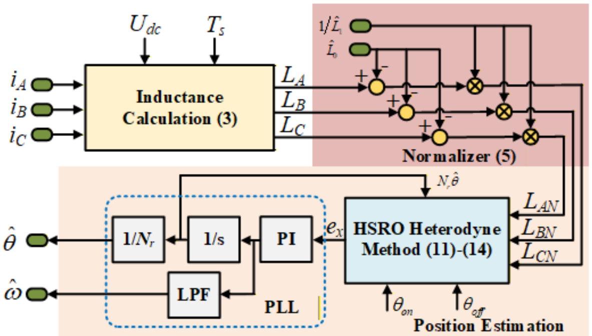

Fig. 4. Overall block diagram of the proposed sensorless control scheme.

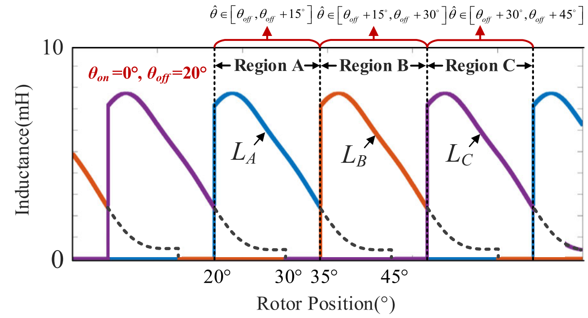

Fig. 5. Idle phase inductance characteristics of a three-phase 12/8 SRM based on the proposed sensorless control scheme.

versus θ shows that within the range of [42°, 45°], $|d\theta/dL|$ is larger than in other regions. It should be noted that the high-sensitivity region (HSR) is a universally present feature in all parameter SRMs due to inductance characteristics. This indicates that, in this HSR shown in Fig. 2, even a minute error in the inductance value will be amplified into a considerable position estimation error.

Therefore, despite the improvement in modeling accuracy, the conventional RPLL-based method is unable to handle the position deviations caused by small disturbances within the HSR, thus failing to meet the high-precision position estimation requirements.

The second drawback is that when the high-frequency pulse signal is injected, a large current amplitude will be excited at the HSR, leading to excessive power losses. The excessive power loss mainly originates from the HFPI in the idle phase. When the injection duration is prolonged, a larger current is generated, resulting in copper losses and additional core losses caused by alternating magnetic flux [35], [36].

III. Proposed Sensorless Control Method

A. Proposed Enhanced Sensorless Control Scheme

Given these limitations mentioned in Section II, the heterodyne method has been refined, and an enhanced sensorless control scheme based on the HSRO heterodyne method is devised. This newly developed approach not only enhances the precision of position estimation simultaneously but also reduces the injection current amplitude, thereby addressing the two limitations of the RPLL scheme. The overall block diagram of the proposed sensorless control scheme is shown in Fig. 4.

The proposed sensorless control scheme first utilizes the calculated idle-phase inductance and combines it with the estimated $\hat{L}_0$ and $\hat{L}_1$ to perform the inductance normalization calculation; then, the relationship between the normalized inductance and the rotor position is established. After clarifying the relationship between the two, an HSRO heterodyne method is employed to extract the total heterodyne signal e_x. The improved heterodyne method addresses the issue of limited accuracy in the conventional RPLL method through optimization. Moreover, the proposed scheme reduces the interval of HFPI, which also leads to a decrease in the amplitude of the injected current, thereby reducing the SRM losses. Finally, the PLL is used to drive the position error e_x to zero and estimate the rotor position and speed for sensorless control. Sections III-B–III-D present detailed description of the key parts of this scheme.

B. HSRO Heterodyne Method

Fig. 5 illustrates the inductance characteristics of the idle phases of a three-phase 12/8 SRM. When any phase is conducted, the corresponding inductance value of that phase is set to zero. The construction steps of the input signal e_x for the PLL based on the improved heterodyne method are as follows.

In region A, only the inductance of phase A is considered, while the inductance of phase C is disregarded. The position information is extracted using a single-phase heterodyne calculation. The estimated position information ranges from θ_{off} to $\theta_{off}+15°$. According to (5), the normalized inductance L_{AN} of phase A is

$$L_{AN} = \frac{L_A - \hat{L}_0 - \hat{L}_2\cos\left(2N_r\hat{\theta}\right)}{\hat{L}_1} = -\cos\left(N_r\theta\right). \qquad (7)$$

To measure the deviation between the actual and estimated rotor position, the phase error $\Delta\phi$ is defined as

$$\Delta\phi = N_r\theta - N_r\hat{\theta} \qquad (8)$$

where $\hat{\theta}_x$ denotes the estimated rotor position for the corresponding phase.

The cosine function can be expanded as

$$\begin{aligned}\cos\left(N_r\theta\right) &= \cos\left(N_r\hat{\theta}+\Delta\phi\right)\\ &= \cos\left(N_r\hat{\theta}\right)\cos\Delta\phi - \sin\left(N_r\hat{\theta}\right)\cdot\Delta\phi. \qquad (9)\end{aligned}$$

When the PLL operates near its locked state, $\Delta\phi$ becomes sufficiently small. The small-angle approximation gives

$$\cos\Delta\phi \approx 1, \quad \sin\Delta\phi \approx \Delta\phi. \qquad (10)$$

Combining (7), (9), and (10) solves the phase error as

$$e_A \triangleq \frac{\cos\left(N_r\hat{\theta}\right) + L_{AN}}{\sin\left(N_r\hat{\theta}\right)} \approx \Delta\phi. \qquad (11)$$

Regarding phases B and C, the same derivation approach as that for phase A can be followed. According to Fig. 5, phase B is utilized for estimating the position within the angular range from $\theta_{off}+15°$ to $\theta_{off}+30°$, while phase C is employed to estimate the position within the angular interval from $\theta_{off}+30°$

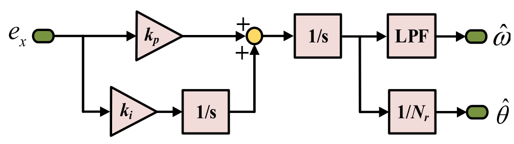

Fig. 6. Design PLL.

to $\theta_{off} + 45°$. The heterodyne signals corresponding to them are as follows:

$$e_B \triangleq \frac{\cos\left(N_r\hat{\theta} + \frac{2\pi}{3}\right) + L_{BN}}{\sin\left(N_r\hat{\theta} + \frac{2\pi}{3}\right)} \approx \Delta\phi \tag{12}$$

$$e_C \triangleq \frac{\cos\left(N_r\hat{\theta} - \frac{2\pi}{3}\right) + L_{CN}}{\sin\left(N_r\hat{\theta} - \frac{2\pi}{3}\right)} \approx \Delta\phi. \tag{13}$$

Based on the derivation logic of phases A, B, and C only involve a fixed phase shift, so e_B and e_C are also equal to $\Delta\phi$. By integrating the heterodyne signals of multiple phases, the expression for the input signal e_x of the PLL is obtained as follows:

$$e_x = \begin{cases} e_A, & \hat{\theta} \in [\theta_{OFF}, \theta_{OFF} + 15°] \\ e_B, & \hat{\theta} \in [\theta_{OFF} + 15°, \theta_{OFF} + 30°] \\ e_C, & \hat{\theta} \in [\theta_{OFF} + 30°, \theta_{OFF} + 45°]. \end{cases} \tag{14}$$

Since the total heterodyne signal e_x continuously and reliably reflects the rotor position error across all sectors, it can be directly used as the PLL input to eliminate this error.

C. Design of PLL

The total heterodyne signal e_x is fed into the PLL for rotor position estimation. As illustrated in Fig. 6, the PLL functions as an angle-tracking observer, from which the rotor position and speed can be extracted.

The corresponding transfer function of the PLL is given as follows:

$$G_{\text{pll}}(s) = \frac{\hat{\theta}(s)}{\theta(s)} = \frac{k_p s + k_i}{N_r s^2 + k_p s + k_i}. \tag{15}$$

Among them, k_p and k_i represent the proportional and integral gains, respectively. A larger k_p enhances the transient response but may introduce overshoot or even destabilize the loop if excessively increased, whereas k_i primarily eliminates the steady-state phase error. Equation (15) shows that the PLL behaves as a second-order system with a single real zero, and the controller gains can be assigned as [34]

$$\begin{cases} k_p = 2\omega_{pll} \\ k_i = \omega_{pll}^2. \end{cases} \tag{16}$$

After the PLL parameters are configured, the PLL is employed to track the demodulated heterodyne signal. When the signal e is regulated by the internal PI controller and driven toward zero, the estimated rotor position $\hat{\theta}$ becomes aligned with the actual rotor position θ, thereby enabling accurate real-time position reconstruction. To suppress the high-frequency components, the demodulated signal is further filtered through a low-pass filter (LPF), after which the rotor speed is computed. The estimated position and speed are subsequently fed back to the heterodyne processing module and the speed controller, forming the complete sensorless closed-loop system.

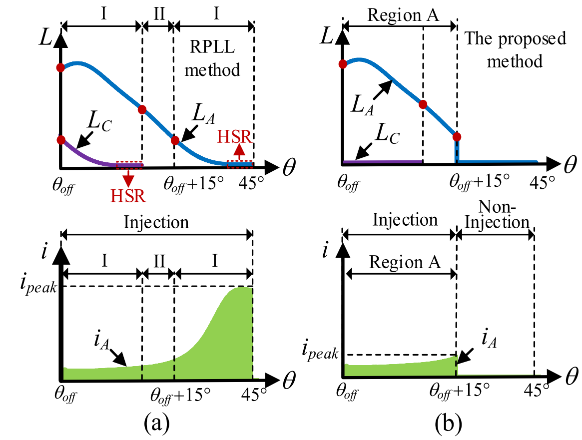

Fig. 7. Schematic illustration of improving precision by avoiding low-inductance region L_C and reducing current amplitude through shortening injection interval. (a) Conventional RPLL method. (b) Proposed method.

D. Comparison With Conventional Heterodyne Scheme

The conventional method requires segmented calculation of the three-phase inductance signals, resulting in high computational complexity. Moreover, in the low inductance region, due to the problem of high sensitivity of the system to small disturbances and the issue of losses caused by the large injected current, its application in scenarios that are sensitive to accuracy is restricted. The improved method overcomes these drawbacks through the following mechanisms.

1) *Improvement of Accuracy:* For the conventional scheme, within region A, there is an overlapping part between L_C and L_A, among which L_C is in the low-inductance region as shown in Fig. 2. The region, as analyzed in Fig. 3, is located at HSR and exhibits a heightened vulnerability to interference, resulting in large position estimation errors. By avoiding the use of L_C in the low-inductance region as shown in Fig. 5, this proposed scheme improves position estimation accuracy.
2) *Reduction of Injection Current:* As the low-inductance region is not utilized, it implies that the injection interval will be shortened. This can reduce the high current amplitude caused by HFPI. Such an optimization strategy can also reduce motor losses and improve the operational efficiency of the SRM. Fig. 7 shows a schematic of the principle to present these advantages visually. In the conventional RPLL scheme depicted in Fig. 7(a), within region I, L_C is in the HSR, which is prone to causing position estimation errors and the injection current has a long interval and high amplitude. In contrast, the proposed method, as shown in Fig. 7(b), only requires a partial range of the single-phase inductance $[\theta_{off}, \theta_{off} + 15°]$ to estimate the position, whereas the conventional RPLL method requires the entire inductance range from $[\theta_{off}, 45°]$. As a result, the injection range is longer, and the injection current amplitude is larger in the conventional RPLL method.

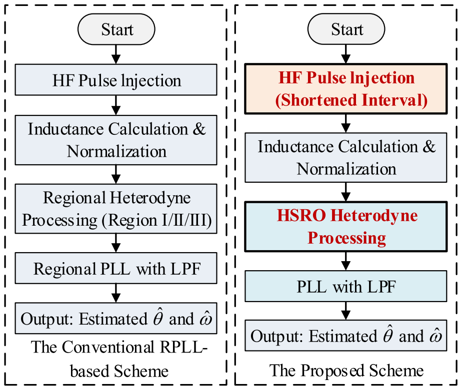

Fig. 8. Flowchart of the conventional RPLL-based and proposed HSRO heterodyne-based sensorless control schemes.

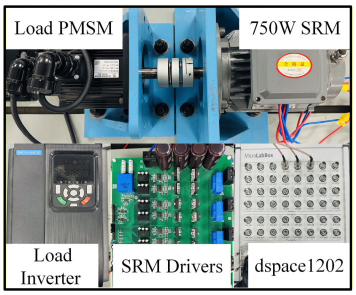

Fig. 9. Three-phase 12/8 SRM experimental setup.

Additionally, Fig. 8 illustrates the process flows of the conventional RPLL-based sensorless control scheme and the proposed HSRO-based scheme, respectively. In the conventional RPLL method, the injection range is longer, and the injection current amplitude is larger. The proposed scheme offers shorter injection intervals and improved estimation accuracy, and its structural enhancement also strengthens robustness against inductance disturbances and parameter uncertainty.

IV. Experimental Verification

To verify the effectiveness and reliability of the proposed low-speed sensorless control scheme, experiments were conducted on a three-phase 750 W, 12/8 SRM setup, as shown in Fig. 9. In the setup, a three-phase permanent magnet synchronous motor (PMSM) is employed as the loading machine. The proposed control algorithm is implemented on a dSPACE1202 real-time control platform, which executes the control tasks at a sampling and switching frequency of 10 kHz. The SRM converter adopts a three-phase asymmetric half-bridge (AHBC) topology using IGW60T120 IGBTs and D100E60 Schottky diodes. The injection period is specifically set to one period, that is, 100 μs.

For a fair comparison, both the benchmark RPLL-based scheme and the proposed HSRO-based scheme are implemented under identical hardware and control settings. The PLL gains are kept the same for both methods, with $k_p = 80$ and $k_i = 1600$, to ensure consistent dynamic response and stability of the heterodyne loop. The activation angles are configured as $\theta_{on} = 0°$ and $\theta_{off} = 20°$ for both schemes to ensure a fair and unbiased comparison, while clearly revealing

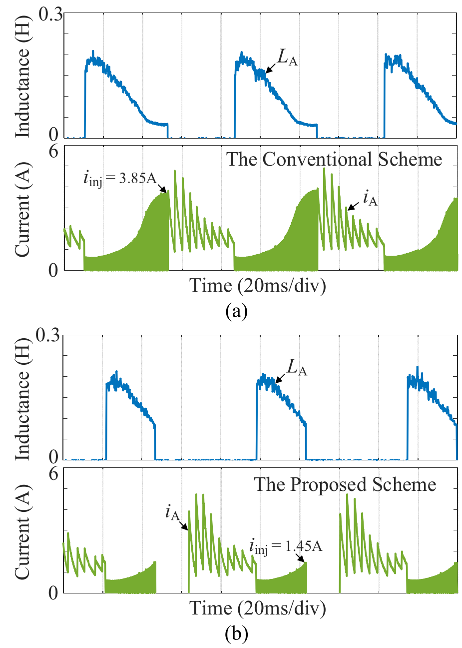

Fig. 10. Comparison experimental results of the idle-phase inductance and phase current at 100 r/min. (a) Conventional RPLL-based scheme. (b) Proposed scheme.

the sensitivity and robustness advantages of the proposed method. The cut-off frequency of the LPF for speed estimation is selected as 15 Hz. All the experiments are carried out strictly in the sensorless control mode, and the experimental data are accurately recorded by the dSPACE 1202 system to ensure the accuracy and reliability of the experimental results. The computation time required for the benchmark RPLL-based scheme is measured at 13 μs, whereas the proposed HSRO-based scheme reduces this to 11.5 μs, representing an approximately 11.5% reduction in computation time.

Fig. 10 illustrates the comparison of experimental results of the idle-phase inductance and phase current between the proposed method and the conventional RPLL-based scheme at 100 r/min. Specifically, Fig. 10(a) corresponds to the conventional RPLL-based scheme, while Fig. 10(b) corresponds to the proposed scheme. During the noninjection interval, the inductance value is set to zero. The phase current diagrams clearly show the dynamic variation trend of the current i_A under the current chopping control and the HFPI control. By comparing Fig. 10(a) with Fig. 10(b), it can be observed that the proposed scheme not only has a shorter injection time but also reduces the peak injection current from 3.85 to 1.45 A (about 63%) compared with the conventional RPLL-based scheme. Due to the additional copper loss caused by high-frequency injection, actual input power measurements are conducted for both injection methods. Under the traditional RPLL-based injection scheme, the input power at no-load increases from 26 W (without injection) to 60 W at 100 r/min, while the proposed scheme only raises it to 44 W. This indicates that under the no-load condition of 100 r/min, the proposed scheme reduces the additional power loss by nearly half compared with the conventional method.

Fig. 11 presents the experimental results of the position comparison and position error between the proposed sensorless

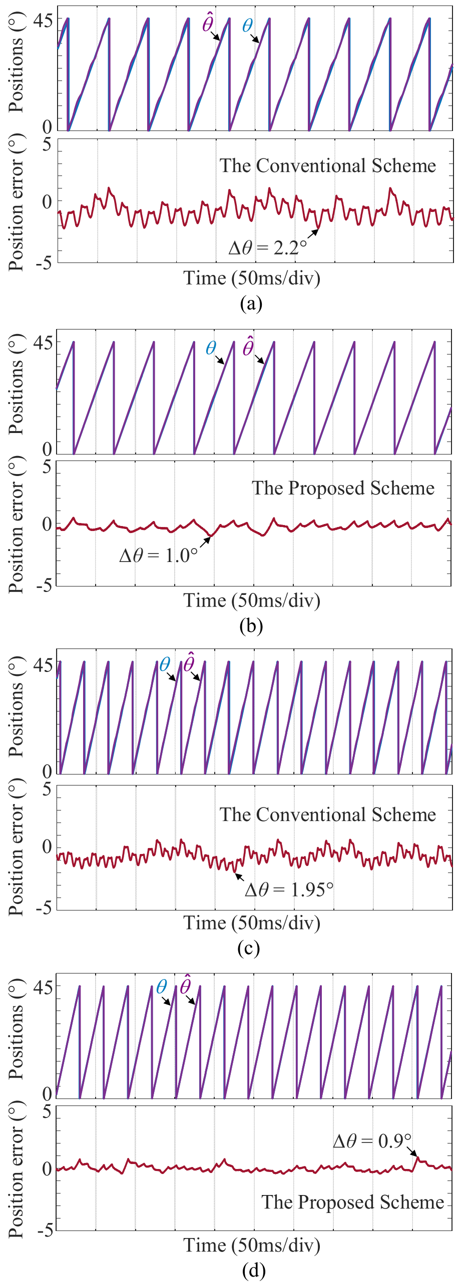

Fig. 11. Experimental results of the position comparison and position error between the proposed sensorless control scheme and the conventional sensorless control scheme based on RPLL at different speeds. (a) Conventional scheme at 150 r/min. (b) Proposed scheme at 150 r/min. (c) Conventional scheme at 250 r/min. (d) Proposed scheme at 250 r/min.

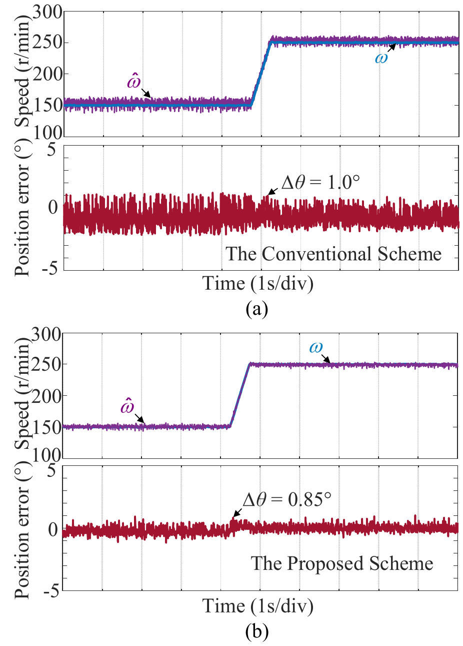

Fig. 12. Comparison of acceleration experiments from 150 to 250 r/min. (a) Conventional RPLL-based scheme. (b) Proposed scheme.

control scheme and the conventional sensorless control scheme based on RPLL at different speeds. In Fig. 11(b) and (d), the proposed scheme at 150 and 250 r/min is shown, respectively. In the upper subplots, the high consistency between the actual rotor position θ and the estimated position $\hat{\theta}$ reflects the qualified position estimation ability of the proposed scheme. The position error $\Delta\theta$ in the lower subplots shows that the position error $\Delta\theta$ is around 1.0° at 150 r/min and 0.9° at 250 r/min. Fig. 11(a) and (c) shows the experimental results of the conventional scheme at 150 and 250 r/min, respectively. As shown in these figures, the position-tracking performance and estimation accuracy of the conventional scheme are lower than those of the proposed scheme. Specifically, the position error $\Delta\theta$ is around 2.2° in (a) and about 1.95° in (c). Overall, under low-speed steady-state conditions, the proposed sensorless control scheme demonstrates advantages in position tracking and estimation accuracy, with an improvement in estimation precision of approximately 50%.

Fig. 12 compares the dynamic response of the proposed sensorless control scheme with the conventional RPLL-based method under a step speed command from 150 to 250 r/min. In Fig. 12(b), corresponding to the proposed scheme, the estimated speed $\hat{\omega}$ closely tracks the actual speed ω during the entire step-up process. The lower subplot shows that the position error $\Delta\theta$ remains tightly bounded, with a peak value of approximately 0.9° during the acceleration interval, indicating robust position-tracking capability under speed transients. In contrast, Fig. 12(a) illustrates the response of the conventional scheme, where the position error exhibits larger oscillations and a higher peak value of about 1.0°, during the acceleration interval.

Fig. 13 illustrates the speed estimation error at 150 and 250 r/min for both the proposed and conventional schemes. Under the proposed scheme, the maximum deviation between the estimated and actual speeds is limited to about 16 r/min at 150 r/min and 11 r/min at 250 r/min, whereas the conventional method exhibits larger errors of approximately 26 and 20 r/min, respectively. This corresponds to a reduction of roughly 40% in the speed estimation error, demonstrating that the proposed sensorless strategy achieves more accurate and robust speed estimation over the tested low-speed operating range. Overall, the proposed sensorless control scheme achieves more accurate position estimation and smoother dynamic performance than the conventional RPLL-based method in the step speed experiment. Table I provides a comprehensive comparison of the key performance metrics

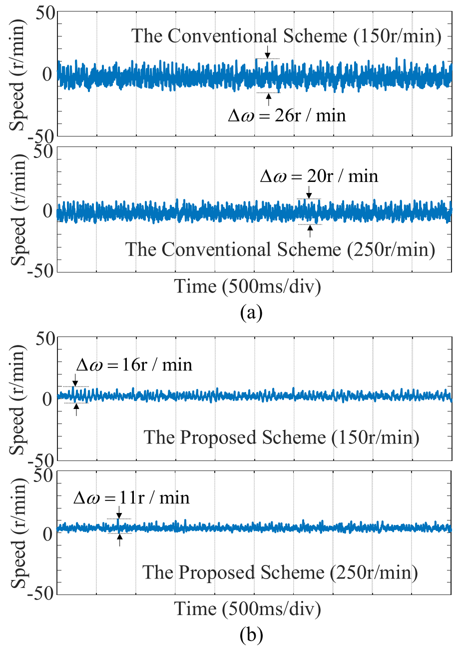

Fig. 13. Comparison of speed estimation error at 150 and 250 r/min. (a) Conventional RPLL-based scheme. (b) Proposed scheme.

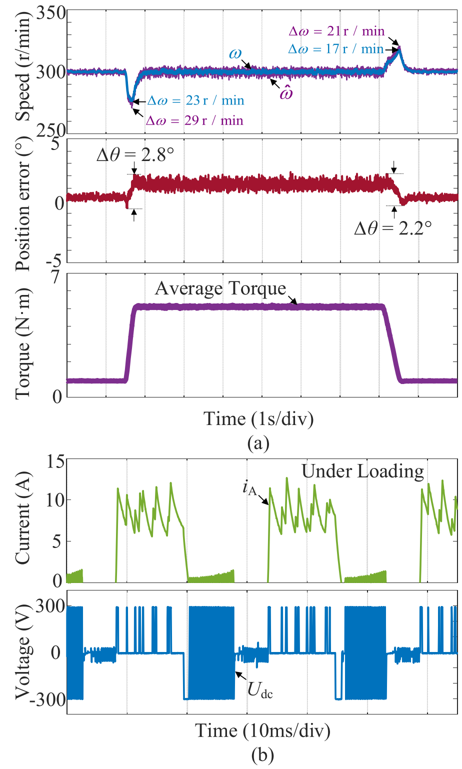

Fig. 14. Proposed sensorless control scheme 300 r/min (20% rated speed) under full load. (a) Speed, position error, and average torque. (b) Current and voltage waveforms under full load.

TABLE I
PERFORMANCE COMPARISON: CONVENTIONAL SCHEME AND PROPOSED SCHEME

Metric	Conventional Scheme	Proposed Scheme
Peak injection current	2.35A	0.80 A
Steady-state position error $\Delta\theta$(150r/min)	2.2°	1.0°
Steady-state position error $\Delta\theta$(250r/min)	1.95°	0.9°
Step-up speed position error $\Delta\theta$(150-250r/min)	1.0°	0.85°
Speed error $\Delta\omega$(150 r/min)	26 r/min	16 r/min
Speed error $\Delta\omega$(250 r/min)	20 r/min	11 r/min

TABLE II
EFFICIENCY COMPARISON AT RATED TORQUE AND 300 R/MIN FOR DIFFERENT METHODS

Method	Rated Torque (N·m)	Efficiency (%)
No Injection	5	38.77%
Proposed Method	5	37.95%
Conventional Method	5	35.24%

for the conventional RPLL-based scheme and the proposed HSRO-based scheme under identical test conditions.

Fig. 14 illustrates the dynamic performance of the proposed sensorless control scheme at 300 r/min (20% of the rated speed) under full-load average torque disturbances of 5 N·m. Fig. 14(a) compares the actual speed ω with the estimated speed $\hat{\omega}$. When the load torque steps from light load to 5 N·m, ω and $\hat{\omega}$ exhibit small transient drops of about 23 and 29 r/min, respectively, but both quickly recover to the steady state value of 300 r/min under the action of the speed controller. A similar behavior is observed during the unloading process, where the speed deviations are approximately 17 r/min for ω and 21 r/min for $\hat{\omega}$, followed again by a fast return to the reference speed. The middle subplot shows the corresponding position error $\Delta\theta$. The peak values of $\Delta\theta$ are about 2.8° during loading and 2.2° during unloading, after which the error rapidly shrinks and remains within a small range. The bottom subplot in Fig. 14(a) presents the applied torque profile, highlighting that the proposed sensorless control algorithm maintains accurate speed and position estimation even when subjected to full-load torque steps. Fig. 14(b) shows the corresponding current and voltage waveforms under full load. These results confirm that the proposed scheme exhibits strong robustness against load disturbances at low speeds. In addition, Table II shows the efficiency comparison at rated torque 5 N·m and 300 r/min for different methods. The proposed method achieves an efficiency of 37.95%, while the no-injection method results in an efficiency of 38.77% and the conventional RPLL method yields 35.24%.

Fig. 15 shows the experimental verification of the proposed sensorless control scheme during a speed-reversal operation. The reference speed is commanded to reverse from +100 to −100 r/min first, and then reverse back to +100 r/min. Throughout the entire transient process, the estimated speed $\hat{\omega}$ tracks the actual speed ω closely. Although a noticeable fluctuation in the position error $\Delta\theta$ appears around each reversal instant, the peak error during the reversal from positive to negative speed is limited to about 4.3°, and the maximum error during the subsequent reversal from negative to positive speed is 4.8°. After each reversal, $\Delta\theta$ converges back to a small steady-state value. Fig. 15(b) shows the corresponding phase current and DC-link voltage waveforms at $|\omega|$ = 100 r/min.

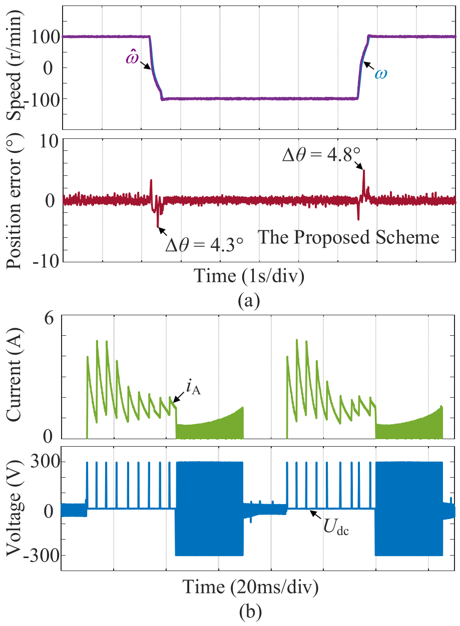

Fig. 15. Experimental verification of the proposed sensorless control scheme during speed reversal. (a) Speed and position error. (b) Current and voltage waveforms at $|\omega|$ = 100 r/min.

These results confirm that the proposed sensorless control scheme works effectively during speed-reversal operations.

V. Conclusion

The proposed enhanced sensorless control scheme improves estimation accuracy and reduces injection current amplitude compared to conventional methods. By adopting the HSRO heterodyne method, the adverse effects of the sensitivity in the low-inductance region are avoided, enabling the proposed sensorless control scheme to achieve around 50% improvement in estimation accuracy. Additionally, due to the shortening of the injection interval, the amplitude of the current excited by HPFI is reduced by 63%, which in turn lowers the motor losses. Extensive experimental validation on a 750 W three-phase SRM setup confirms the reliability and effectiveness of the proposed scheme, establishing its superior control performance.

Acknowledgment

The authors acknowledge the supports from Wilson Tang Brilliant Energy Science and Technology Laboratory (BEST Laboratory) at The Hong Kong University of Science and Technology (Guangzhou).

References

[1] L. Ge et al., “Advanced technology of switched reluctance machines in more electric aircraft: A review,” *IEEE Trans. Power Electron.*, vol. 40, no. 1, pp. 195–216, Jan. 2025.

[2] Y. Shao, Y. Yu, and F. Chai, “Dual closed-loop position observer with nonlinearity-decoupled model for feature- flux-based sensorless SRM drives,” *IEEE Trans. Ind. Electron.*, vol. 71, no. 1, pp. 160–170, Jan. 2024.

[3] Z. Chen et al., “Autoswitching ADRC-based approach for enhanced speed control and torque ripple minimization in switched reluctance motors,” *IEEE Trans. Ind. Electron.*, vol. 72, no. 10, pp. 9953–9963, Oct. 2025.

[4] X. Sun, N. Wang, M. Yao, and G. Lei, “Position sensorless control of switched reluctance motors based on angle adjustment using nonlinear inductance and flux model,” *IEEE Trans. Ind. Electron.*, vol. 71, no. 12, pp. 15467–15477, Dec. 2024.

[5] X. Guo, S. Zeng, R. Zhong, and W. Hua, “High-precision injection current sampling scheme for direct drive low-speed position sensorless control of switched reluctance machine,” *IEEE Trans. Ind. Electron.*, vol. 71, no. 11, pp. 13754–13765, Nov. 2024.

[6] X. Guo, S. Zeng, R. Zhong, and W. Hua, “Automatic offline measurement of full-cycle unsaturated inductance for low-speed rotor position estimation in switched reluctance machines,” *IEEE J. Emerg. Sel. Topics Power Electron.*, vol. 12, no. 1, pp. 849–861, Feb. 2024.

[7] Q. Sun, T. Lan, X. Liu, S. Li, F. Niu, and C. Gan, “Linear inductance model reshaping-based sensorless position estimation method for SRM with antimagnetic saturation capability,” *IEEE J. Emerg. Sel. Topics Power Electron.*, vol. 11, no. 5, pp. 4799–4807, Oct. 2023.

[8] D. Zhou, H. Chen, X. Wang, V. F. Pires, and J. Martins, “Synthetic sensorless control scheme for full-speed range of switched reluctance machine drives with fault-tolerant capability,” *IEEE Trans. Transport. Electrific.*, vol. 8, no. 4, pp. 4456–4469, Dec. 2022.

[9] C. Gan, Y. Chen, Q. Sun, J. Si, J. Wu, and Y. Hu, “A position sensorless torque control strategy for switched reluctance machines with fewer current sensors,” *IEEE/ASME Trans. Mechatronics*, vol. 26, no. 2, pp. 1118–1128, Apr. 2021.

[10] J. Ye, B. Bilgin, and A. Emadi, “Elimination of mutual flux effect on rotor position estimation of switched reluctance motor drives considering magnetic saturation,” *IEEE Trans. Power Electron.*, vol. 30, no. 2, pp. 532–536, Feb. 2015.

[11] Z. Chen, H. Jing, X. Wang, L. Ge, Z. Song, and D. Xiao, “High-speed sensorless control strategy of SRMs: Utilizing fourth order generalized integrator to enhance control performance and overcome magnetic characteristic constraints,” *IEEE Trans. Ind. Appl.*, vol. 61, no. 1, pp. 335–344, Jan. 2025.

[12] Z. Chen et al., “General-purpose high-speed position-sensorless control of switched reluctance motors using single-phase adaptive observer,” *IEEE Trans. Transport. Electrific.*, vol. 10, no. 3, pp. 5241–5249, Sep. 2024.

[13] Z. Chen et al., “Selective harmonic elimination and dynamic enhancement in magnetic-characteristic-free sensorless control of SRM drives at high speeds,” *IEEE Trans. Power Electron.*, vol. 39, no. 5, pp. 5339–5348, May 2024.

[14] D. Lv, W. Ding, S. Chen, J. Cai, and Z. Yin, “Sensorless control scheme for SRM drives using Newton–Raphson method-based finite position set-phase locked loop,” *IEEE J. Emerg. Sel. Top. Power Electron.*, early access, Nov. 17, 2025, doi: 10.1109/JESTPE.2025.3633267.

[15] X. Sun, N. Wang, M. Yao, and G. Lei, “Position sensorless control of SRMs based on improved sliding mode speed controller and position observer,” *IEEE Trans. Ind. Electron.*, vol. 72, no. 1, pp. 100–110, Jan. 2025.

[16] H. Wang, J. Du, Z. Niu, and Y. Xue, “Estimating rotor position for SRM via regional sliding mode observer,” *IEEE Trans. Ind. Electron.*, vol. 72, no. 1, pp. 230–239, Jan. 2025.

[17] A. Yalavarthi and B. Singh, “Sensorless speed control of SRM drive using optimized neural network model for rotor position estimation,” *IEEE Trans. Energy Convers.*, vol. 39, no. 4, pp. 2158–2168, Dec. 2024.

[18] Y. Zhao, J. Zhu, P. Ren, H. Cao, and S. Zhang, “Position-sensorless control of SRM drives based on a novel super-twisting sliding mode observer with the machine learning model,” *IEEE J. Emerg. Sel. Topics Power Electron.*, vol. 13, no. 5, pp. 6178–6189, Oct. 2025.

[19] Y. Cai, Y. Wang, H. Xu, S. Sun, C. Wang, and L. Sun, “Research on rotor position model for switched reluctance motor using neural network,” *IEEE/ASME Trans. Mechatronics*, vol. 23, no. 6, pp. 2762–2773, Dec. 2018.

[20] J. Bu and L. Xu, “Eliminating starting hesitation for reliable sensorless control of switched reluctance motors,” *IEEE Trans. Ind. Appl.*, vol. 37, no. 1, pp. 59–66, Jan. 2001.

[21] A. Sarr, I. Bahri, D. Diallo, and E. Berthelot, “Sensorless control of switched reluctance machine,” in *Proc. 42nd Annu. Conf. IEEE Ind. Electron. Soc. (IECON)*, Oct. 2016, pp. 6693–6698.

[22] H. Cheng, H. Chen, S. Xu, and S. Yang, “Four-quadrant sensorless control in switched reluctance machine drive using pulse injection based on special flux linkage curves,” *IET Electric Power Appl.*, vol. 11, no. 9, pp. 1566–1574, Nov. 2017.

[23] X. Guo, S. Zeng, R. Zhong, and W. Hua, “Online self-commissioning of unsaturated inductance characteristics for low-speed position sensorless control in switched reluctance machines,” *IEEE Trans. Ind. Electron.*, vol. 71, no. 6, pp. 5576–5585, Jun. 2024.

[24] J. Shao, Z. Deng, and Y. Gu, "Fault-tolerant control of position signals for switched reluctance motor drives," *IEEE Trans. Ind. Appl.*, vol. 53, no. 3, pp. 2959–2966, May 2017.

[25] I. Ralev, S. Max, and R. W. De Doncker, "Accurate rotor position detection for low-speed operation of switched reluctance drives," in *Proc. IEEE 18th Int. Power Electron. Motion Control Conf. (PEMC)*, Aug. 2018, pp. 483–490.

[26] J. Cai and Z. Deng, "Unbalanced phase inductance adaptable rotor position sensorless scheme for switched reluctance motor," *IEEE Trans. Power Electron.*, vol. 33, no. 5, pp. 4285–4292, May 2018.

[27] X. Guo, S. Zeng, M. Wu, R. Zhong, and W. Hua, "A low-speed position sensorless scheme from standstill for low-cost SRM drives based on triple current slope difference threshold," *IEEE Trans. Ind. Electron.*, vol. 71, no. 4, pp. 3296–3306, Apr. 2024.

[28] J. Cai and Z. Liu, "An unsaturated inductance reconstruction based universal sensorless starting control scheme for SRM drives," *IEEE Trans. Ind. Electron.*, vol. 67, no. 11, pp. 9083–9092, Nov. 2020.

[29] X. Sun, Y. Zhu, Y. Cai, Z. Zhu, and Y. Xiong, "Speed sensorless control of switched reluctance motors in full-speed range based on inductance characteristics," *IEEE Trans. Transport. Electrific.*, vol. 10, no. 2, pp. 4018–4028, Jun. 2024.

[30] L. Zhang, Y. Yu, and Z. Xin, "A position estimation for switched reluctance motor using full cycle envelope," in *Proc. IEEE 3rd Inf. Technol. Mechatronics Eng. Conf. (ITOEC)*, Oct. 2017, pp. 909–913.

[31] J. Kim, J.-M. Choe, S. Moon, and J.-S. Lai, "Position sensorless control of switched reluctance motor drives without pre-stored magnetic characteristics," in *Proc. IEEE Energy Convers. Congr. Expo. (ECCE)*, Portland, OR, USA, Sep. 2018, pp. 1755–1761.

[32] D. Xiao, J. Ye, G. Fang, Z. Xia, X. Wang, and A. Emadi, "A regional phase-locked loop-based low-speed position-sensorless control scheme for general-purpose switched reluctance motor drives," *IEEE Trans. Power Electron.*, vol. 37, no. 5, pp. 5859–5873, May 2022.

[33] D. Xiao et al., "Induced current reduction in position-sensorless SRM drives using pulse injection," *IEEE Trans. Ind. Electron.*, vol. 70, no. 5, pp. 4620–4630, May 2023.

[34] D. Lv, W. Ding, Y. Wang, S. Chen, J. Cai, and X. Wu, "Low-speed sensorless control of switched reluctance motor drives using random pulse injection for noise reduction," *IEEE Trans. Transport. Electrific.*, vol. 11, no. 1, pp. 5005–5016, Feb. 2025.

[35] H. Chen et al., "Research on iron loss of switched reluctance starter/generator for energy storage," *Protection Control Modern Power Syst.*, vol. 9, no. 4, pp. 147–159, Jul. 2024.

[36] H. Chen, W. Yan, and K. Wang, "Iron loss analysis of double-sided linear switched reluctance launcher," *IEEE Trans. Plasma Sci.*, vol. 47, no. 5, pp. 2323–2330, May 2019.

Zifeng Chen (Graduate Student Member, IEEE) received the B.S. degree in measurement and control technology and instrument from Shenyang University of Technology, Shenyang, China, in 2018, and the M.S. degree in automation and control from Newcastle University, Newcastle upon Tyne, U.K., in 2020. He is currently pursuing the Ph.D. degree in sustainable energy and environment with The Hong Kong University of Science and Technology (Guangzhou), Guangzhou, China.

He is affiliated with the Department of Mechanical and Aerospace Engineering, The Hong Kong University of Science and Technology, Hong Kong, China. His research interests include motor drives and control.

Xijian Lin received the M.S. degree in electrical engineering from the School of Automation, Guangdong University of Technology, Guangzhou, China, in 2023. He is currently pursuing the Ph.D. degree in sustainable energy and environment with The Hong Kong University of Science and Technology (Guangzhou), Guangzhou.

His research interests include motor drive and battery management systems.

Dehui Luo (Graduate Student Member, IEEE) received the B.S. degree in electrical engineering from The University of British Columbia, Vancouver, BC, Canada, in 2021, and the M.Sc. degree in sustainable energy and environment from The Hong Kong University of Science and Technology (Guangzhou), Guangzhou, China, where he is currently pursuing the Ph.D. degree in same program.

His research focuses on advanced control methods for electric drive systems and robotic applications.

Molong Duan (Member, IEEE) received the B.S. degree in theoretical and applied mechanics from Peking University, Beijing, China, in 2012, and the M.S. and Ph.D. degrees in mechanical engineering from the University of Michigan, Ann Arbor, MI, USA, in 2013 and 2018, respectively.

He has been an Assistant Professor with the Department of Mechanical and Aerospace Engineering, The Hong Kong University of Science and Technology, Hong Kong, SAR, China, since 2021. His research interests include the modeling and control of dynamic systems, robotic manufacturing systems, additive manufacturing control, continuous fiber additive manufacturing, and flexible aircraft modeling and control.

Dr. Duan has received multiple international best paper and poster awards for his contributions to the field.

Shun Cai (Member, IEEE) was born in Hubei, China. He received the B.Eng. and M.Sc. degrees from Zhejiang University, Hangzhou, China, in 2014 and 2017, respectively, and the Ph.D. degree from the University of Sheffield, Sheffield, U.K., in 2020, all in electrical engineering.

He currently serves as a Researcher with Zhejiang University. Prior to that, he was a Research Fellow with Nanyang Technological University, Singapore, a Senior Engineer with Dyson Technology Ltd., Malmesbury, U.K., and an Assistant Professor with University College London, London, U.K. His major research interests include electrical machine and drive systems, advanced propulsion systems, and high-precision actuator systems.

Dianxun Xiao (Senior Member, IEEE) received the B.S. and M.S. degrees in electrical engineering from Harbin Institute of Technology, Harbin, China, in 2016 and 2018, respectively, and the Ph.D. degree in electrical and computer engineering from McMaster University, Hamilton, ON, Canada, in 2021.

He is currently an Assistant Professor with the Sustainable Energy and Environment Thrust, The Hong Kong University of Science and Technology (Guangzhou), Guangzhou, China, and also affiliated with The Hong Kong University of Science and Technology, Hong Kong, SAR, China. Before that, he was a Post-Doctoral Research Fellow with the McMaster Automotive Resource Centre, McMaster University, Hamilton, ON, Canada, in 2021. His research interests include permanent magnet synchronous motor drives, switched reluctance motor drives, high-power converters, and battery management systems for transportation electrification applications.

Dr. Xiao severs as an Associate Editor for IEEE TRANSACTIONS ON TRANSPORTATION ELECTRIFICATION. He received the IEEE IAS The Myron Zucker Student-Faculty Grant in 2024.